

1 Beam Position Reconstruction for the g2p Experiment
2 in Hall A at Jefferson Lab

3 Pengjia Zhu^{a,*}, Kalyan Allada^{b,g}, Trent Allison^b, Toby Badman^c, Alexandre
4 Camsonne^b, Jian-ping Chen^b, Melissa Cummings^d, Chao Gu^e, Min Huang^f,
5 Jie Liu^e, John Musson^b, Karl Slifer^c, Vincent Sulkosky^{e,g}, Yunxiu Ye^a, Jixie
6 Zhang^{b,e}, Ryan Zielinski^c

7 ^a*University of Science and Technology of China, Hefei, Anhui 230026, China*

8 ^b*Thomas Jefferson National Accelerator Facility, Newport News, VA 23606, USA*

9 ^c*University of New Hampshire, Durham, NH 03824, USA*

10 ^d*College of William & Mary, Williamsburg, VA 23187, USA*

11 ^e*University of Virginia, Charlottesville, VA 22904, USA*

12 ^f*Duke University, Durham, NC 27708, USA*

13 ^g*Massachusetts Institute of Technology, MA, 02139, USA*

14 **Abstract**

Beam-line equipment was upgraded for experiment E08-027 (g2p) in Hall A at Jefferson Lab. Two beam position monitors (BPMs) were necessary to measure the beam position and angle at the target. A new BPM receiver was designed and built to handle the low beam currents (50-100 nA) used for this experiment. Two new super-harps were installed for calibrating the BPMs. In addition to the existing fast raster system, a slow raster system was installed. Before and during the experiment, these new devices were tested and debugged, and their performance was also evaluated. In order to achieve the required accuracy (1-2 mm in position and 1-2 mrad in angle at the target location), the data of the BPMs and harps were carefully analyzed, as well as reconstructing the beam position and angle event by event at the target location. The calculated beam position will be used in the data analysis to accurately determine the kinematics for each event.

15 **Keywords:** g2p; BPM; raster; beam position

*Corresponding author

Email address: pzhu@jlab.org, zhupj55@mail.ustc.edu.cn (Pengjia Zhu)

16 **1. Introduction**

17 A polarized ammonia (NH_3) target was used for the first time in Hall A for
18 the g2p experiment [1]. It operated at a low temperature of 1K and a strong
19 transverse magnetic field of either 5 T or 2.5 T. A high electron beam current
20 would cause significant target polarization drop due to target temperature rising
21 and ionization radiation to the target material [2]. To minimize depolarization,
22 the beam current was limited to below 100 nA and a raster system was used
23 to spread the beam spot out to a larger area. The transverse magnetic field
24 in the target region would cause the beam to be deflected downward when the
25 beam enters the target region. To compensate for this, two chicane magnets
26 were placed in front of the target to pre-bend the beam upwards. Due to the
27 low beam current and tight space limitations after the chicane magnets, the
28 experimental accuracy goals for the position (1-2 mm) and angle (1-2 mrad) at
29 the target were challenging to achieve. New beam-line devices and an associated
30 readout electronics system were designed for the g2p experiment to accomplish
31 these goals. Design details and the performance of the beam-line devices will be
32 described in the following sections along with a discussion of an analysis method
determine the beam position and direction.

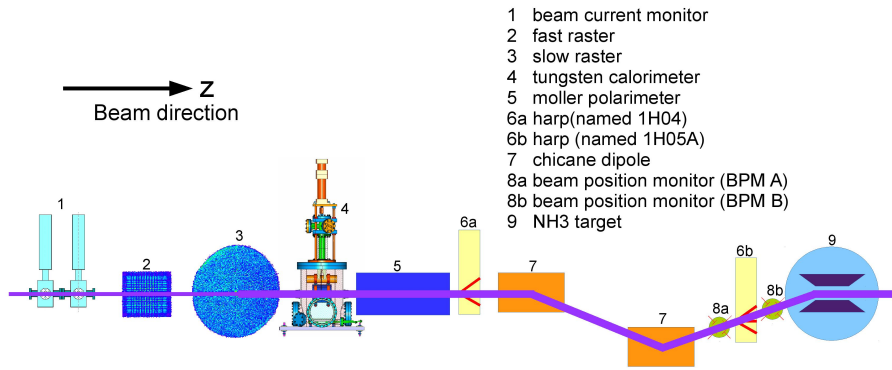


Figure 1: Schematic of beamline components for g2p experiment

34 **2. Beam-line Instrumentation**

35 *2.1. Beam position monitor (BPM)*

36 The scattering angle of the outgoing lepton in deep inelastic scattering, which
37 is defined with respect to the direction of the incident beam, is an important
38 variable for obtaining meaningful physics results. Therefore, the position and
39 direction of the beam, after being bent by the chicane magnetic field and spread
40 out by the rasters, must be measured precisely. Two BPMs and two harps were
41 installed for relative and absolute measurements of beam position and direction
42 near the target, respectively.

43 The BPM consists of four open-ended antennas for detecting the beam po-
44 sition; the measurement is non-invasive to the beam. The BPM chambers
45 shown in Fig.2 are part of the beam pipe. The four antennas are attached
46 to feedthroughs on the interior wall of the pipe at 90° intervals. The BPM

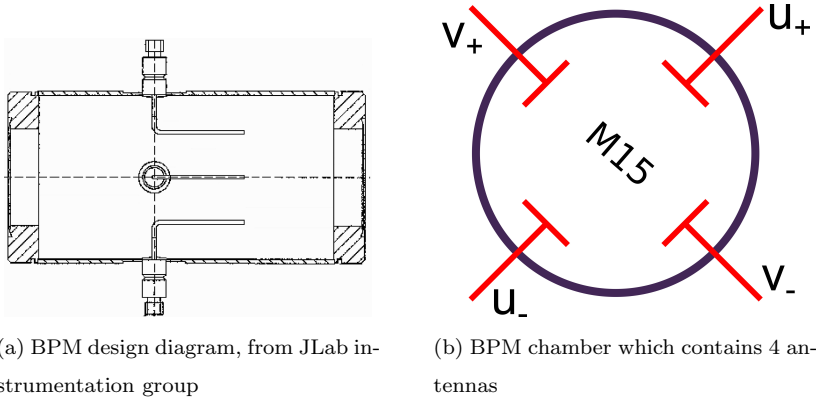


Figure 2: BPM chamber

46
47 chambers are placed with a 45° rotation (along z) with respect to the global
48 Hall coordinate. The two pairs of antennas are marked as u_+ , u_- and v_+ , v_- ,
49 respectively, which are used to determine beam positions in u and v directions.
50 When the beam passes through the BPM chamber, each antenna receives an
51 induced signal. The BPM front-end receiver collects and sends the signal to
52 the regular Hall A DAQ system and another DAQ system designed for parity

53 violation experiments, the HAPPEX system [3]. The new BPM receiver was
54 designed by the JLab instrumentation group [4] in order to achieve the required
55 precision at a level of 0.1 mm with a beam current as low as 50 nA. The regular
56 DAQ system was connected to a 13-bit fastbus ADC (Lecroy ADC 1881) with
57 an integration time of 50 ns, which was triggered by a scattered electron event.
58 The HAPPEX system was connected to an 18-bit ADC with an integration
59 time of 875 μ s, which was triggered by a beam helicity signal at 1 kHz. The
60 amplitude, A , recorded in the ADC has the following relation with the BPM
61 signal, ϕ :

$$A \propto \phi \cdot 10^{g/20}, \quad (1)$$

62 where g is the gain of the receiver.

63 The BPM receiver generates a large time delay for the output signals. The
64 digital filter used in the receiver contributes 1/175 s delay time, which was the
65 inverse of the bandwidth setting chosen for the filter. There is a $\sim 4 \mu$ s delay
66 as a result of finite processing times. The BPM cannot provide event by event
67 position because of these time delays, due to the 25 kHz fast raster system.

68 Because of the space limitation between the second chicane magnet and the
69 target, the two BPMs were placed close to each other. One was placed 95.5 cm
70 upstream of the target while the other was placed 69 cm upstream, making the
71 distance between them only 26.5 cm. The short distance magnified the position
72 uncertainty from the BPMs to target.

73 *2.2. Super harp*

74 Two super harps were designed and installed in the beam-line, as shown in
75 Fig.1 (label 6a - 1H04 and 6b - 1H05A), to provide an absolute measurement
76 of the beam position for calibration of the BPMs. The new harps were able to
77 work in pulsed beam (1% duty factor) with a current of several μ A. A diagram
78 for the harp is shown in Fig.3, which consists of three wires with a thickness of
79 50 μ m, a fork and a controller chassis. The harp chamber is perpendicular to
80 the beam pipe and connected to the beam pipe as part of the vacuum chamber

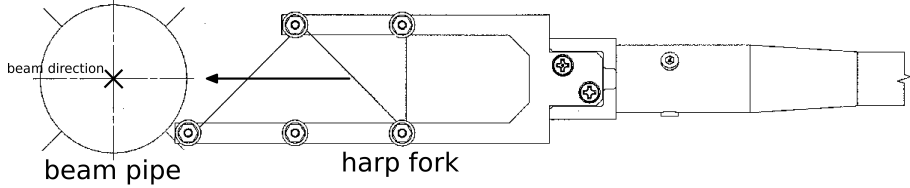


Figure 3: Harp diagram

81 of the beamline. The two harps have different configurations of three wires:
 82 vertical(|), bank left(\), and bank right(/) for 1H04, and /, |, \ for 1H05. The
 83 angle of the / or \ wire is 45° relative to the wire dock frame. The wires are
 84 arranged in a fork (Fig.3) controlled by a step motor [5] which can be moved in
 85 and out of the beam-line. The harps must be moved out of the beam-line when
 86 production data is being taken because they are invasive to the beam. The
 87 original position of the wires was surveyed before the experiment at a precision
 88 level of 0.1 mm. As the motor driver moved the fork through the beam, each
 89 wire received a signal, which was recorded for further analysis. The signals
 90 received from the wire and the step-counters from the motor driver were then
 91 sent to an amplifier and the DAQ. The amplification and the speed of the motor
 92 were adjustable for the purpose of optimizing the signals of each scan. Recorded
 93 data combined with the survey data were used to calculate the absolute beam
 94 position.

95 The signal from the | wire ($peak_{|}$) was used for getting the x position (x_{harp})
 96 of the beam, and the signals from the /, \ wires ($peak_{/}$ and $peak_{\backslash}$) were used
 97 for getting the y position (y_{harp}):

$$\begin{aligned} x_{harp} &= survey_{|} - peak_{|} \\ y_{harp} &= \frac{1}{2}[(survey_{\backslash} - survey_{/}) - (peak_{\backslash} - peak_{/})] \end{aligned} \quad (2)$$

98 2.3. Raster system

99 In order to minimize the depolarization, avoid damage to the target material
 100 from radiation, and reduce systematic error for the polarization measurement
 101 by NMR (The polarization of the NH_3 target was measured by using a NMR

102 coil which was placed inside the target cell [6], and the non-uniformity of de-
 103 polarization could reduce the precision of the NMR measurement due to the
 104 measurement being an average over the target), two raster systems were in-
 105 stalled at ~ 17 m upstream of the target, as shown in Fig.1 (labels 2 and 3 for
 106 fast and slow rasters, respectively). Both the fast and slow rasters consist of
 107 two dipole magnets. The same triangular waveforms with frequency of 25 kHz
 108 were used to drive the magnet coils of the fast raster to move the beam in x and
 109 y directions, forming a rectangular pattern of about $2 \text{ mm} \times 2 \text{ mm}$, as shown in
 Fig.4.

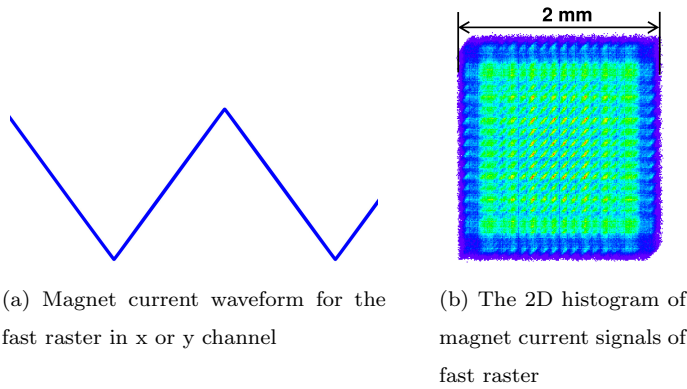


Figure 4: Fast raster pattern

110
 111 A dual-channel function-generator¹ was used to generate two independent
 112 waveforms to drive the magnet coils of the slow raster. The waveforms for the
 113 x and y directions are:

$$\begin{aligned}
 x &= A_x t^{1/2} \sin(\omega t), \\
 y &= A_y (t + t_0)^{1/2} \sin(\omega t + \phi),
 \end{aligned} \tag{3}$$

114 where the A_x and A_y are the maximum amplitude, t_0 and ϕ are the AM and

¹agilent 33522A function generator, <http://www.home.agilent.com/en/pd-1871286-pn-33522A/function-arbitrary-waveform-generator-30-mhz>

sin phase difference between x and y waveform, respectively. Both of them

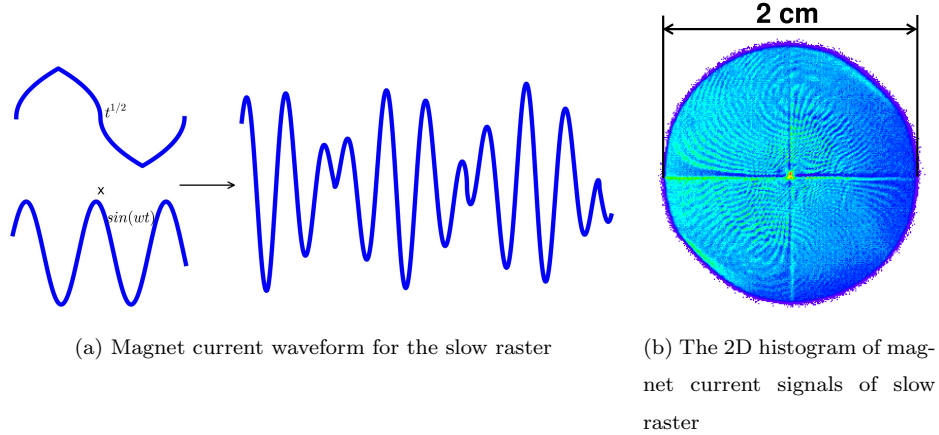
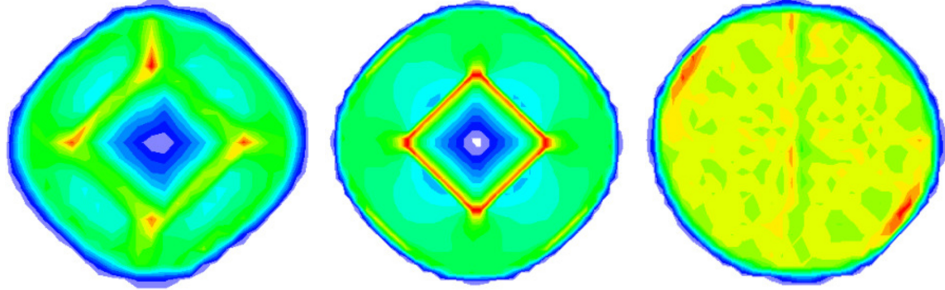


Figure 5: Slow raster pattern

115
 116 are sine functions modulated by a function $t^{1/2}$ in order to generate a uniform
 117 circular pattern [7], as shown in Fig.5. The frequencies of the x and y waveforms
 118 kept same: $\omega = 99.412$ Hz. In order to cycle the amplitude modulation (AM)
 119 function, four piece-wise functions are combined together. The first term is $t^{1/2}$,
 120 and the second term is $period - t^{1/2}$, and so on for the third and fourth terms.
 121 The cycled function has the frequency of 30 Hz.

122 The ϕ was locked to $\frac{\pi}{2}$ by the function generator, while the t_0 was manually
 123 fixed to 0. Non-zero t_0 could cause a non-uniformity pattern, as shown in
 124 Fig.6(a), which would cause non-uniformity beam distribution. A simulation
 125 was reproduced the non-uniformity by setting the t_0 to non-zero, as shown
 126 in Fig.6(b). The t_0 was carefully adjusted and minimized before production
 127 data taking to avoid the non-uniformity. The pattern of the spread beam was
 128 relatively uniform after this adjustment during the experiment, as shown in
 129 Fig.6(c).



(a) Raster pattern with $t_0 \neq 0$ (b) Simulated raster pattern, (c) Manually adjust t_0 to 0 with $t_0 \neq 0$

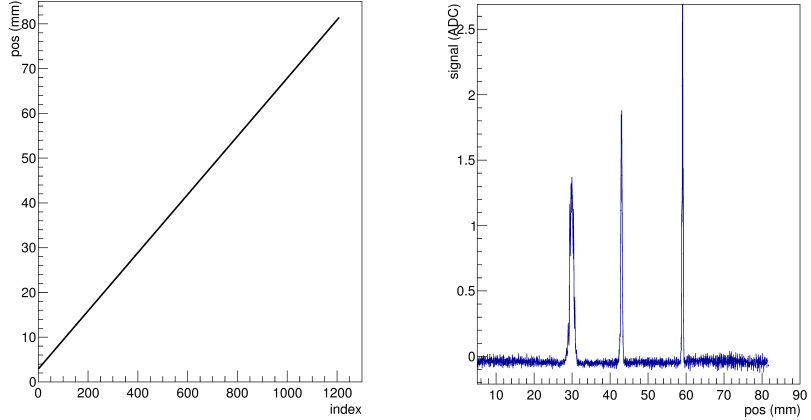
Figure 6: None-zero t_0 caused slow raster non-uniformity, (a) and (c) are from the data recorded in the ADC, (b) is simulated. The color palette shows the uniformity of the raster pattern.

130 **3. Data analysis**

131 *3.1. Harp scans for measuring absolute beam position*

132 An example of a harp scan result is shown in Fig.7. There are three groups of
133 recorded data for each harp scan, which are “index”, “position”, and “signal”.
134 The index is related to the moving steps of the fork during the scan. Each
135 step of the index increases by 0.008-0.07 mm depending on the speed of the
136 motor driver [5]. The position is the wire location for each index. The testing
137 results show a good linear relation between the position and the index as shown
138 in Fig.7(a), because the motor speed is uniform. The line is the fitted result
139 with $pos = a * index + b$. According to this linear relation, interpolation or
140 extrapolation can be applied when a few data points are missing, in some cases.
141 The strength of signal vs. position is plotted in Fig.7(b). Each peak represents
142 the location when one of the three wires passed through the beam.

143 The positions measured by the two harps were used for calibrating the beam
144 positions in the two BPMs. When the chicane magnets were on, beam did not
145 pass straight through from the first harp to the second harp. BPM calibrations
146 using two harps were only possible when the chicane magnets were off, i.e. in the



(a) position vs index for harp scan, used for extending position record

(b) Signal vs position for harp, x axis is position, y axis is the strength of signal, which is the ADC value.

Figure 7: 1H05A harp scan data

147 straight-through settings. Since the BPM was calibrated in the local coordinate
 148 system, the calibration constants were independent from the settings of other
 149 instruments. To make sure that the calibration constants for the BPMs were
 150 still valid during the non-straight-through settings, the settings for the BPM
 151 receiver were kept the same as in the straight-through settings during production
 152 running.

153 The scan data from the harps were not reliable when the current of CW
 154 beam (100% duty factor) was lower than 100 nA due to the low signal-to-noise
 155 ratio. The harp scans were taken in pulsed mode at a current of a few μ A, while
 156 the BPMs were used for production data taking in CW mode at a beam current
 157 of 50-100 nA. For a BPM calibration run, a harp scan was done first in pulsed
 158 mode, then a DAQ run was taken immediately to record the ADC value in CW
 159 mode without changing the beam position. The harp scan was then taken again
 160 in the pulsed mode to double check the beam position. The harp scan data was
 161 discarded and the scan was taken again if the beam position changed.

162 3.2. BPM data analysis and calibration

163 The traditional difference-over-sum (Δ/Σ) method of calculating the beam
 164 position has the non-linearity effect at the position far away from the center of
 165 the beam pipe [8]. It is necessary to correct the equation of Δ/Σ since we have a
 166 slow raster with a large size of ~ 2 cm. With the assumption of an infinitely long
 167 chamber and neglecting the antenna influence on the electric field inside the
 168 chamber, the signal from each antenna excited by the beam can be calculated
 169 via image charge method (Fig.8) [9, 10] :

$$\phi_i = \phi_0 I \frac{R^2 - \rho^2}{R^2 + \rho^2 - 2R\rho\cos(\theta_i - \theta_0)}, \quad (4)$$

170 where ϕ_i is the signal received in the antenna, and i is u_+ , u_- , v_+ and v_- ,
 171 respectively, ϕ_0 is a constant related to the geometry of the BPM-chamber and
 172 the output resistance, I is the beam current, R is the radius of the BPM vacuum
 173 chamber, ρ is the radial position of the beam, and $\theta_i - \theta_0$ is the angle difference
 between the antenna and the beam in the polar coordinate .

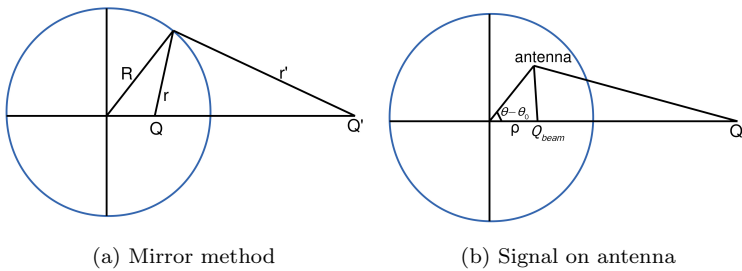


Figure 8: Signal for each antenna of BPM

174
 175 In order to extract the beam position information, and eliminate the depen-
 176 dence on the beam current in equation (4), the Δ/Σ method is used as follows:

$$D_U = \frac{\phi_{U+} - \phi_{U-}}{\phi_{U+} + \phi_{U-}}, \quad (5)$$

177 where U denotes u and v . Substituting equation (4) into equation (5), it can be
 178 rewritten as follows:

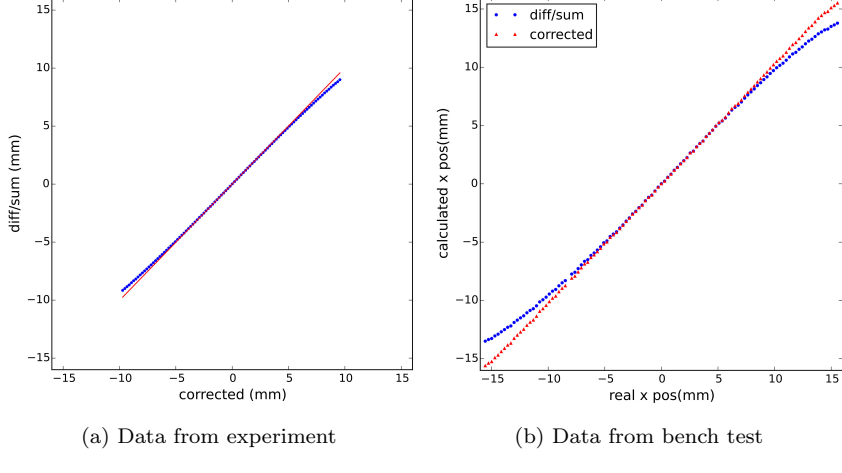


Figure 9: BPM non-linearity correction. (a) Comparison between the position calculated from Δ/Σ equation (7) (y axis) and the one from correction equation (8) (x axis). Red solid line is a reference line came from linear fit of the center points. Data is collected from the experiment. (b) Comparison between the Δ/Σ equation (7) and the correction equation (8) using the bench test data. The x axis is the real beam position. The red triangles are the positions calculated from correction equation (8). The blue circles are the positions calculated from Δ/Σ equation (7) .

$$D_U = \frac{\phi_{U+} - \phi_{U-}}{\phi_{U+} + \phi_{U-}} = \frac{2}{R} \frac{\rho \cos(\theta - \theta_0)}{1 + \frac{\rho^2}{R^2}} = \frac{2}{R} \frac{U}{1 + \frac{\rho^2}{R^2}}, \quad (6)$$

where $\rho^2 = u^2 + v^2$. When $u^2 + v^2 \ll R^2$, equation (6) is simplified as:

$$U \approx \frac{R}{2} D_U = \frac{R}{2} \frac{\phi_{U+} - \phi_{U-}}{\phi_{U+} + \phi_{U-}}. \quad (7)$$

Equation (7) can be used in the simple case when the beam is near the center of the beam pipe. When the beam is far from the center, equation (7) is no longer valid. For the g2p experiment, the beam was rastered to have a diameter of about 2 cm at the target. From equation (6) the beam position is calculated as:

$$U = RD_U \left(\frac{1}{D_u^2 + D_v^2} - \frac{1}{\sqrt{D_u^2 + D_v^2}} \sqrt{\frac{1}{D_u^2 + D_v^2} - 1} \right). \quad (8)$$

185 The correction equation is tested by using the experiment data and the bench
 186 test data. Fig.9(a) shows the comparison between the position calculated from
 187 the correction equation (8) and the one from the Δ/Σ equation (7). The red
 188 solid line is a reference line came from linear fit of the center points. Fig.9(b)
 189 shows the comparison with the real beam position from the bench test data.
 190 In this way the method using equation (8) can correct the non-linearity effect
 191 caused by the Δ/Σ method. The handling of the BPM information which only
 192 used for the center beam position (discussed in chapter 3.4) also reduced this
 193 non-linearity effect.

194 The final information recorded in the data-stream was designed to have a
 195 linear response with the raw signal in the 50-100nA current range. The ϕ_i in
 196 equation (6) can be rewritten as:

$$\phi_i = a_i(A_i - A_{i-ped} + b_i), \quad (9)$$

197 where A_i and A_{i-ped} are the recorded ADC value and pedestal value, and a_i and
 198 b_i are the slope and intercept of the relationship between ϕ_i and $A_i - A_{i-ped}$.
 199 Equation (7) can be rewritten as:

$$D_U = \frac{(A_{U+} - A_{U+ped} + b_{U+}) - h_U(A_{U-} - A_{U-ped} + b_{U-})}{(A_{U+} - A_{U+ped} + b_{U+}) + h_U(A_{U-} - A_{U-ped} + b_{U-})}, \quad (10)$$

200 where $h_U = a_{U-}/a_{U+}$, which is related to the ratio of the signals from the U_+
 201 and U_- antennas and the gain settings of the two channels.

202 Combining the equations (9) and (4), the calibration constant b_i was ob-
 203 tained by taking the linear fit between the ADC values of BPM and the beam
 204 current: $I \propto (A_i - A_{i-ped} + b_i)$. Besides, the linear fit used a group of runs which
 205 had the same beam position but different beam current. Figure 10 shows the
 206 $A_i - A_{i-ped}$ versus the beam current. It shows that the ADC values were linear
 207 with beam current in the considering current range of 50-100 nA. The intercept
 208 from the linear fit of Fig.10 is the value b_i .

209 By transporting the position x_{harp} and y_{harp} in equation (2) from two harps
 210 to the BPM local coordinate u_{harp} and v_{harp} , a fit between the BPM data U

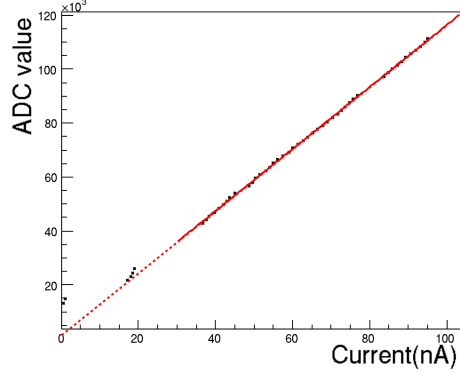


Figure 10: ADC value of BPM raw signal ($A - A_{ped}$) V.S. beam current

and the harp data U_{harp} determined three calibration constants c_0 , c_1 and c_2 :

$$U_{harp} = U_c = c_0 + c_1 u + c_2 v, \quad (11)$$

where U_c is the calibrated BPM position. It was converted to Hall coordinate X_c for further transporting to the target location. An calibration example is shown in Fig.11. The asterisks and the dots in Fig.11 represent U_{harp} and U ,

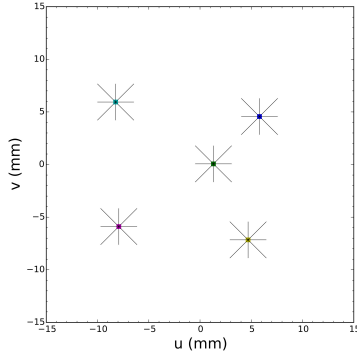


Figure 11: Harp scan data combined with BPM data, the asterisks are the positions from harp, while the dots are from BPM.

respectively.

In order to reduce the noise and improve the resolution during data analysis, a software filter was applied. Since the 18 bit ADC was triggered by the helicity

218 signal with a fixed frequency, it could be regarded as a sampling ADC. Fig.12
219 shows the signal dealt with a 2 Hz low pass filter. Three plots at the bottom of
220 Fig.12 (a,b) are the averaged signal used for comparing with the filtered signal.
221 The results show that the 2 Hz filter and the 0.5 s average are consistent within
222 the required precision. The filter also erases the beam displacement caused by
223 the rasters, which is necessary to extract the position of the beam center.

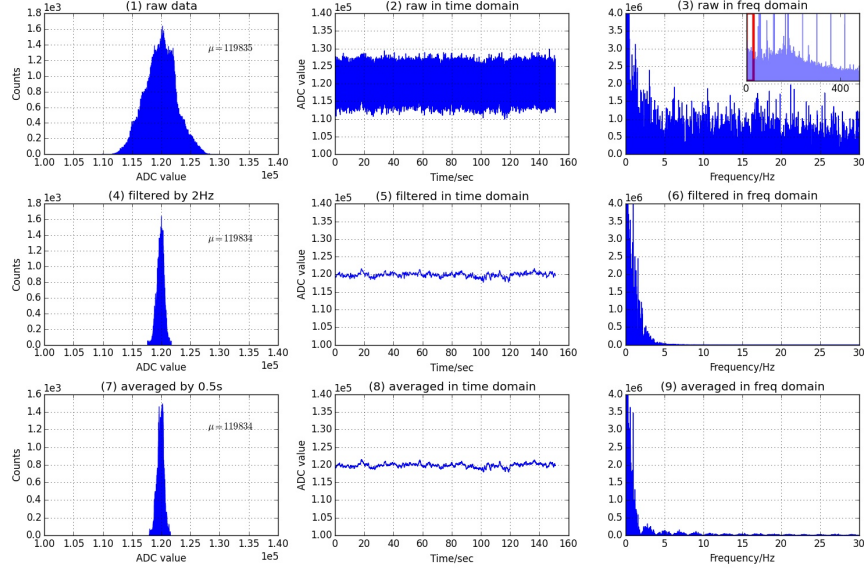
224 *3.3. Beam position reconstruction at the target*

225 It is easy to transport the position from the BPMs to the target by using a
226 linear transportation method for the straight through setting. For the settings
227 with a transverse magnetic field at the target, the linear transportation method
228 cannot be used since the beam is bent near the target. A target magnet field
229 map [11] was generated from the TOSCA model. To test the accuracy of the
230 TOSCA model, the target magnet field was measured before the experiment
231 [12, 13]. The position and angle at target were calculated in terms of the
232 positions at BPMA and BPMB, together with the magnet field information.
233 Fits were used to speed up the calculation. To do this, a full simulation was
234 taken by generating thousands of trajectories with different initial positions and
235 angles. The fits were compared with the full simulation and they are consistent
236 with negligible difference. Fig.13 shows the trajectories from the simulation.

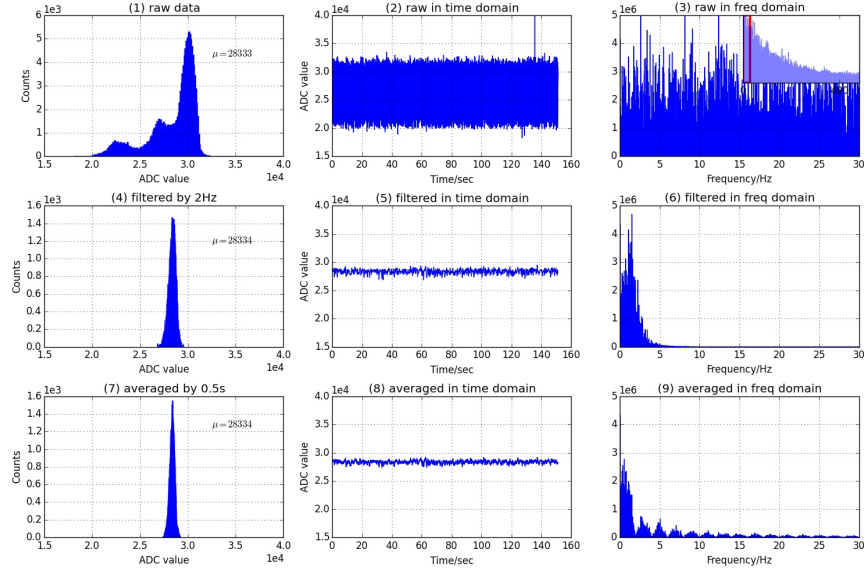
237 The fitted transport functions were only used to transport the beam center
238 position from the two BPMs to the target by applying the 2 Hz filter, which
239 filtered out the fast raster and slow raster motion to keep only the beam center
240 position. The transported position were expressed as X_{center} .

241 *3.4. Determining the beam position event-by-event*

242 The readout of the magnet current for the two rasters was connected to
243 a series of ADCs. Two scintillator planes in the HRS form a DAQ trigger.
244 This pulse signal triggered the ADC to record the raster magnet current for
245 each event. The information from the rasters and the BPMs was combined



(a) Normal run with beam



(b) Pedestal run without beam

Figure 12: Software filter applied to BPM signal. (a) is the signal with beam, (b) is the pedestal signal without beam. (1,2,3) in (a,b) are the raw signal without applying the filter, (4,5,6) are applied a 2 Hz finite-impulse-response filter with 4th order. (7,8,9) are averaged with 0.5 s. (1,4,7) are the 1-D histogram of the recorded signal, (2,5,8) are the signal in time domain, (3,6,9) are in frequency domain. Note all of the plots in (a) are from a single signal, same as in (b).

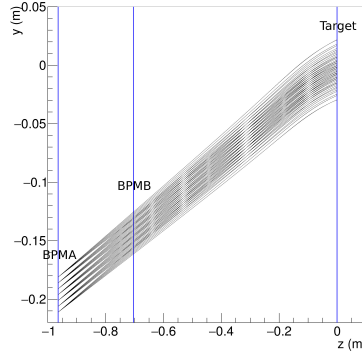


Figure 13: Transporting beam position from BPM to target with transverse target magnet field. Trajectories are from simulation. Blue lines show the z positions of BPMA, BPMB and target. y and z are in global Hall coordinate.

²⁴⁶ to provide the beam position event-by-event. The position at the target was
²⁴⁷ determined as:

$$X = X_{center} + X_{fstraster} + X_{slraster}, \quad (12)$$

²⁴⁸ where $X_{fstraster}$ and $X_{slraster}$ were the position displaced by the fast raster
²⁴⁹ and slow raster, respectively, which were converted from the current values of
²⁵⁰ the two raster magnets. The calibration of the conversion factors between the
²⁵¹ magnet current of the rasters and the displaced position will be discussed in the
²⁵² next subsection. An example of reconstructed beam position is shown in Fig.14.

²⁵³

²⁵⁴ 3.4.1. Conversion factor for the slow raster

²⁵⁵ Two methods were used to calibrate the conversion factor for the slow raster.
²⁵⁶ The first method used the calibrated BPM information, i.e., comparing the
²⁵⁷ raster magnet current with the beam shape shown in the ADC of the BPMs.
²⁵⁸ Several calibrations were taken during different run periods at a beam current of
²⁵⁹ 100nA using different values of the raster magnet current, as shown in Fig.15(a).

²⁶⁰

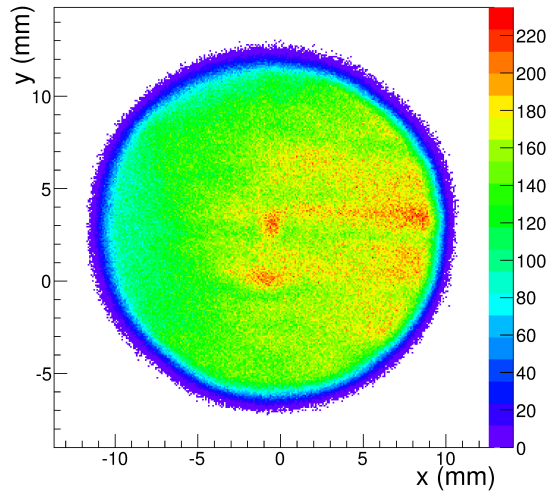


Figure 14: Reconstructed beam position at the target

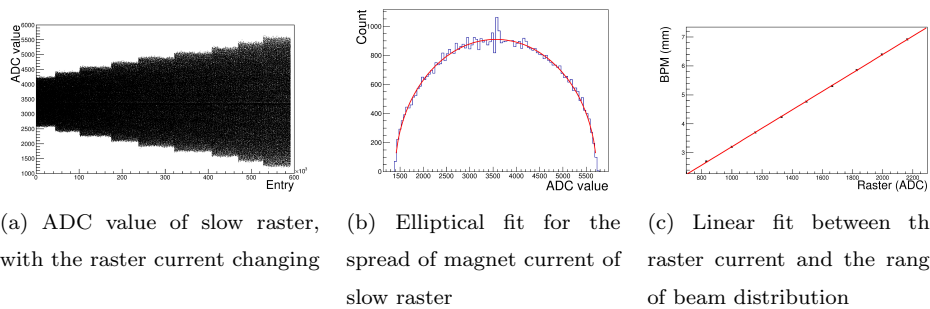


Figure 15: Converting the raster current to beam position shift

261 The range of the beam distribution at the target was calculated from the
 262 ranges at the two BPMs without applying the filter, using the transport func-
 263 tions fitted previously. The range of the beam distribution at the two BPMs
 264 and the amplitude of the raster current were calculated from elliptical fits. An
 265 example of the fit is shown in Fig.15(b). Figure 15(c) shows a linear fit between
 266 the raster current and the range of the beam distribution at the target. The x
 267 axis in Fig.15(c) is the magnet current of the raster, and the y axis is the range
 268 of the beam distribution obtained from the BPMs.

269 The second method for calibrating the conversion factor used a target called
 “carbon hole” as shown in Fig.16(a). Scattered electrons were used as the

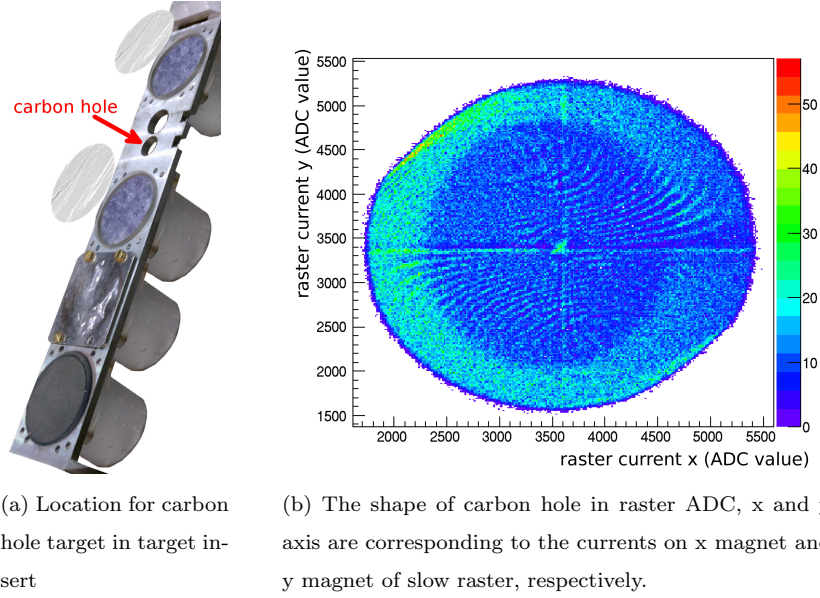


Figure 16: Carbon hole method to calibrate raster

270
 271 trigger for recording the raster magnet current. Since the density of the target
 272 frame was much higher than that of the “hole”, which was submerged in liquid
 273 helium, the density of events triggered from the target frame was much higher
 274 than that of the hole itself. Recorded values reveal a hole shape as shown in
 275 Fig.16(b). The size of the carbon hole was surveyed before the experiment, and
 276 a fit program was used to extract the radius of the recorded hole shape for that

²⁷⁷ raster current. The conversion factor F was then calculated as the ratio of the
²⁷⁸ size of the carbon hole S_{hole} and the radius of the hole shape R_{hole} in the ADC:

$$F = \frac{S_{hole}}{2 * R_{hole}}. \quad (13)$$

²⁷⁹ *3.4.2. Conversion factor for the fast raster*

²⁸⁰ The conversion for the fast raster was the same as for the slow raster. The
²⁸¹ low pass filter for the BPM was set to a higher value than the frequency of the
²⁸² fast raster to see the beam shape at the BPM formed by the fast raster. For a
²⁸³ higher frequency filter, a larger beam current was needed to get a clear pattern.
²⁸⁴ The beam current chosen for calibrating the fast raster was near 300 nA, which
²⁸⁵ was the safety limit for the target. The beam shape formed by the fast raster
is shown in Fig.17.

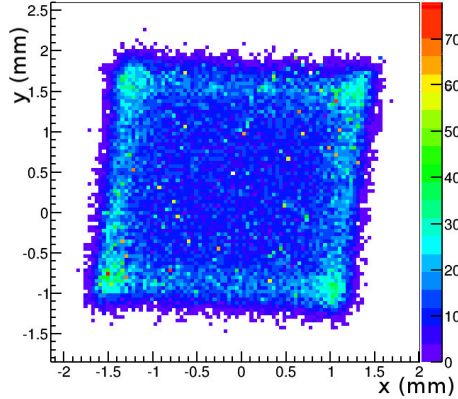


Figure 17: Beam shape formed by the fast raster at the BPM A location, the unit is millimeter

²⁸⁶

²⁸⁷ **4. Uncertainty**

²⁸⁸ The uncertainty of the final beam position at the target for each event con-
²⁸⁹ tains several contributions:

- ²⁹⁰ • The first part comes from the uncertainty of the calibration constant. It
²⁹¹ includes the BPM resolution for the DAQ runs used for the calibration,

292 the uncertainty of the harp data corresponding to each calibration, and
293 the survey uncertainties for the BPMs and harps. It contributes about 0.7
294 mm for the uncertainty of the position and 0.7 mrad for the uncertainty
295 of the angle.

- 296 • The uncertainty on the pedestal is the largest uncertainty for the beam
297 position measurement, contributing about 0.7~1.5 mm to the uncertainty
298 of the position and 0.7~1.5 mrad to the uncertainty of the angle.
- 299 • The uncertainties from the BPM survey need to be included, since the
300 production data and the calibration data were taken at different beamline
301 settings when the equipment was moved. They contribute 0.5 mm to the
302 uncertainty of the position.
- 303 • The uncertainty from the magnetic field map of the target was considered
304 for the settings with the target magnet field.
- 305 • The uncertainties due to the size conversion of the rasters were also in-
306 cluded.

307 The position uncertainty was magnified by a factor of 5 at the target because of
308 the short distance between the two BPMs. For example, in the straight through
309 setting, if the uncertainty at BPM A is 0.2 mm, and at BPM B is 0.27 mm,
310 the uncertainty at the target is 1.1 mm for position and 1.3 mrad for angle.
311 The uncertainty for the position at the target was around 1~2 mm, while the
312 uncertainty for the angle was 1~2 mrad.

313 **5. Summary**

314 JLab g2p experiment used a transversely polarized NH_3 target for the first
315 time in Hall A. It put a limit of below 100 nA on the electron beam current and
316 required a slow raster to spread beam to a large area. Two chicane magnets were
317 used to compensate the strong transverse magnetic field. Beam-line equipment,
318 including the BPMs, harps and associated readout system, were upgraded to

319 allow precision measurements of the beam position at low current (50-100 nA).
320 A software filter was used to reduce noise of the BPMs. A correction equation
321 was used to compensate the non-linearity caused by the Δ/Σ equation. The
322 harp data and the linear fit between the bpm signal and the beam current
323 were used to extract the calibration constant of the BPM. To account for the
324 strong target magnetic field effect, transport functions were fitted to transport
325 the beam position from the BPMs to the target. The beam position in the
326 x-y plane and the angle at the target location are extracted event-by-event by
327 combining information from the BPMs and the signals from the rasters. The
328 performance of the new devices (BPMs, harps and slow rasters) were presented
329 along with an analysis of systematic uncertainties.

330 **Acknowledgments**

331 This work was supported by DOE contract DE-AC05-84ER40150 under
332 which the Southeastern Universities Research Association (SURA) operates the
333 Thomas Jefferson National Accelerator Facility, and by the National Natural
334 Science Foundation of China (11135002, 11275083), the Natural Science Foun-
335 dation of Anhui Education Committee (KJ2012B179).

336 **Reference**

- 337 [1] A. Camsonne, J. P. Chen, D. Crabb and K. Slifer, spokesperson, JLab
338 E08-027 (g2p) experiment.
- 339 [2] D. G. Crabb, W. Meyer, Solid polarized targets for nuclear and particle
340 physics experiments, *Annu. Rev. Nucl. Part. Sci.* 47 (1997) 67–109.
- 341 [3] R. Michaels, Precision Integrating HAPPEX ADC, JLab Technical report
342 (unpublished).
- 343 URL [http://hallaweb.jlab.org/parity/prex/adc18/prex_adc18_](http://hallaweb.jlab.org/parity/prex/adc18/prex_adc18_spec.ps)
344 `spec.ps`

- 345 [4] J. Musson, Functional Description of Algorithms Used in Digital Receivers,
346 JLab Technical report No. JLAB-TN-14-028.
- 347 [5] C. Yan and et al., Superharp - A wire scanner with absolute position read-
348 out for beam energy measurement at CEBAF, Nuclear Instruments and
349 Methods in Physics Research A 365 (1995) 261–267.
- 350 [6] J. Pierce, J. Maxwell, T. Badman, J. Brock, C. Carlin, D. Crabb, D. Day,
351 C. Keith, N. Kvaltine, D. Meekins, J. Mulholland, J. Shields, K. Slifer,
352 Dynamically polarized target for the and experiments at jefferson lab,
353 Nuclear Instruments and Methods in Physics Research Section A: Acceler-
354 ators, Spectrometers, Detectors and Associated Equipment 738 (0) (2014)
355 54 – 60. doi:<http://dx.doi.org/10.1016/j.nima.2013.12.016>.
356 URL [http://www.sciencedirect.com/science/article/pii/
357 S0168900213016999](http://www.sciencedirect.com/science/article/pii/S0168900213016999)
- 358 [7] C. Yan, Hall C Polarized Target Raster System Upgrade, JLab Technical
359 report (unpublished).
360 URL https://www.jlab.org/Hall-C/talks/01_06_05/yan.pdf
- 361 [8] W. Barry, A general analysis of thin wire pickups for high fre-
362 quency beam position monitors, Nuclear Instruments and Meth-
363 ods in Physics Research Section A: Accelerators, Spectrometers,
364 Detectors and Associated Equipment 301 (3) (1991) 407 – 416.
365 doi:[http://dx.doi.org/10.1016/0168-9002\(91\)90004-A](http://dx.doi.org/10.1016/0168-9002(91)90004-A).
366 URL [http://www.sciencedirect.com/science/article/pii/
367 016890029190004A](http://www.sciencedirect.com/science/article/pii/016890029190004A)
- 368 [9] C.R.Carman, J. L. Pellegrin, The beam positions of the spear storage ring,
369 SLAC-PUB-1227.
- 370 [10] P.Poit, Evaluation and correction of nonlinear effects in fnpl beam position
371 monitors, FNPL Technical report No.Beams-doc-1894-v1.
372 URL [http://beamdocs.fnal.gov/AD-public/DocDB>ShowDocument?
373 docid=1894](http://beamdocs.fnal.gov/AD-public/DocDB>ShowDocument?docid=1894)

- ³⁷⁴ [11] R. Wines, private communication.
- ³⁷⁵ [12] J. Liu, Magnetic field mapping on a translation table, JLab Technical
³⁷⁶ report, E08-027 Collaboration (unpublished).
- ³⁷⁷ URL http://hallaweb.jlab.org/experiment/g2p/collaborators/jie/2011_10_05_fieldmap_report/Target_Field_Report.pdf
- ³⁷⁹ [13] C. Gu, Target field mapping and uncertainty estimation, JLab Technical
³⁸⁰ report, E08-027 Collaboration (unpublished).
- ³⁸¹ URL https://hallaweb.jlab.org/experiment/g2p/collaborators/chao/technotes/Chao_TechNote_TargetField.pdf